



Self-Assembled Propylammonium Cations at Grain Boundaries and Film Surface to Improve Efficiency and Stability of Perovskite Solar Cells

Journal:	<i>Journal of Materials Chemistry A</i>
Manuscript ID	TA-COM-02-2019-001755.R1
Article Type:	Communication
Date Submitted by the Author:	29-Mar-2019
Complete List of Authors:	Fei, Chengbin; University of Miami, Department of physics Zhou, Meng; University of Miami, Physics Ogle, Jonathan; University of Utah Smilgies, Detlef; Cornell University, CHESS Whittaker-Brooks, Luisa; University of Utah, Chemistry Wang, He; University of Miami, Physics

COMMUNICATION

Self-Assembled Propylammonium Cations at Grain Boundaries and Film Surface to Improve Efficiency and Stability of Perovskite Solar Cells

Received 00th January 20xx,
Accepted 00th January 20xx

DOI: 10.1039/x0xx00000x

Chengbin Fei,^a Meng Zhou,^a Jonathan Ogle,^b Detlef-M. Smilgies,^c Luisa Whittaker-Brooks^b and He Wang^{*a}

The major challenge of bringing organic-inorganic hybrid perovskite solar cells towards commercialization is their inherent instability especially with regards to moisture. The introduction of a small amount of hydrophobic cation of large size into a 3D perovskite structure which typically aids in the formation of a quasi-2D perovskite structure has been shown to be a promising method for maintaining high efficiency while introducing a high stability toward moisture. By comparing a family of different cations, the propylammonium (PA) cation is found to be the most effective at mitigating these instability issues. Via femtosecond transient absorption and reflection spectroscopy, the large cations are found to preferentially accumulate at the grain boundaries and film surface, forming heterostructures and preventing moisture penetration. The preferential crystal orientation, crystallization, and grain size in both lateral and vertical directions are enhanced accordingly, in particular when PA is incorporated into the perovskite active layer. Such self-assembled large cations suppress the charge recombination and enhance device efficiency. Along with enhancements to efficiency, the addition of the PA cation significantly improves both device and precursor stabilities.

Introduction

The power conversion efficiency of organic-inorganic hybrid perovskite (OIHP) solar cells has achieved 23.7%, on par with the efficiency of commercial silicon solar cells.¹ The main challenges towards the commercialization of OIHP solar cells are their thermal, oxygen, light, and moisture instabilities.²⁻⁴ In particular, the OIHP tends to change gradually into the “hydrated perovskite phases” upon exposure to moisture and finally decomposes after a long time.⁵⁻⁷ The moisture-induced

degradation usually starts from the film surface and grain boundaries.⁸ Therefore, developing a means to prevent the degradation at the surface and grain boundaries is of paramount importance. Recent attempts have focused on the development and utilization of 2D OIHP materials due to the increased hydrophobic property of organic cations with larger sizes.⁹⁻¹² According to the tolerance factor for 3D OIHPs, the cation is limited to methylammonium (MA), formamidinium (FA), Cs or their mixture.^{2, 13} When the size of cation becomes larger, such as butylammonium (BA) and phenethylammonium (PEA), quantum-well like 2D structures are formed.^{14, 15}

Contrary to 3D OIHPs, 2D OIHPs promote long-term stability, but sacrifice device performance due to poorer carrier mobility and larger exciton binding energies.¹⁶⁻¹⁸ The pursuit of simultaneously efficient and stable photovoltaic cells has led to mixtures of 2D and 3D OIHPs, referred to as quasi-2D OIHPs. Surprisingly, by optimizing the composition, it is found that the addition of a small amount of large cations¹⁹⁻²¹ or fluorinated cations^{22, 23} not only improves the moisture stability, but also increases device efficiency. The efficiency improvement is attributed to the passivation of grain boundaries, preferential crystal orientation, higher crystallization, and phase stabilization. For example, by adding small amounts of BA or PEA into MA or FA, the large cations form at the grain boundaries without disrupting the 3D crystal structure.²⁴ As such, these cations can passivate interfacial trap sites and suppress non-radiative charge recombination.²⁵⁻²⁷ Besides the commonly used doping method, quasi-2D OIHPs can be prepared via an organic-cation displacement approach, which converts the perovskite from 2D PA₂PbI₄ to 3D MAPbI₃ structure.^{28, 29} Furthermore, the 2D perovskite can also enable the 3D crystallites to be oriented normal to the substrate to assist out-of-plane charge carrier transport.³⁰⁻³² 3D OIHPs such as formamidinium lead iodide (FAPbI₃) tend to degrade from a black phase to a yellow phase, especially in the case of a single type of cation (not mixed with MA and Cs). Recently, it has been demonstrated that the incorporation of BA or PEA into FA can also stabilize 3D OIHP structure containing a pure FA phase to prolong their stability when incorporated into a photovoltaic device.^{33, 34}

^a Department of Physics, University of Miami, Coral Gables, Florida 33146, United States. E-mail: hewang@miami.edu

^b Department of Chemistry, University of Utah, Salt Lake City, Utah 84112, United States.

^c Cornell High Energy Synchrotron Source, Cornell University, Ithaca, New York 14853, United States.

Electronic Supplementary Information (ESI) available: [details of any supplementary information available should be included here]. See DOI: 10.1039/x0xx00000x

Despite all the advances achieved in optimizing the device efficiency of quasi-2D OIHPs, most efforts so far have been mainly focused on selecting BA and PEA as large cations to form quasi-2D OIHPs. Although a small amount of the large cation is expected to segregate at the film surface to prevent moisture penetration, it has not been straightforward to observe such segregation, and how this capping layer affects the surface carrier dynamics remains unclear. In this study, we compare the effects of different large cations such as, ethylammonium (EA), n-propylammonium (PA) and BA cations on the performance and stability of quasi-2D OIHP photovoltaic devices. Our results indicate that the incorporation of a small amount of PA into the hybrid perovskite active layer aids in the improvement of solar cell performance and stability. To understand such enhancement,

spectroscopy to compare the carrier dynamics in the bulk and at the surface. Our findings suggest that large cations preferentially accumulate at the film surface. We determined that the crystal preferential orientation, crystallinity, lateral and vertical grain sizes all increase with the incorporation of large cations in particular for PA. This suppresses carrier recombination and prolongs carrier lifetime, ultimately improving device efficiency and stability.

Results and discussion

The chemical formula of a quasi-2D OIHP is $A_2B_{n-1}Pb_nX_{3n+1}$, where n represents the number of inorganic layers between organic layers.^{35, 36} We use EA, PA, or BA as spacer cation A, a mixture of MA, FA, and Cs as cation B, a mixture of Br and I as

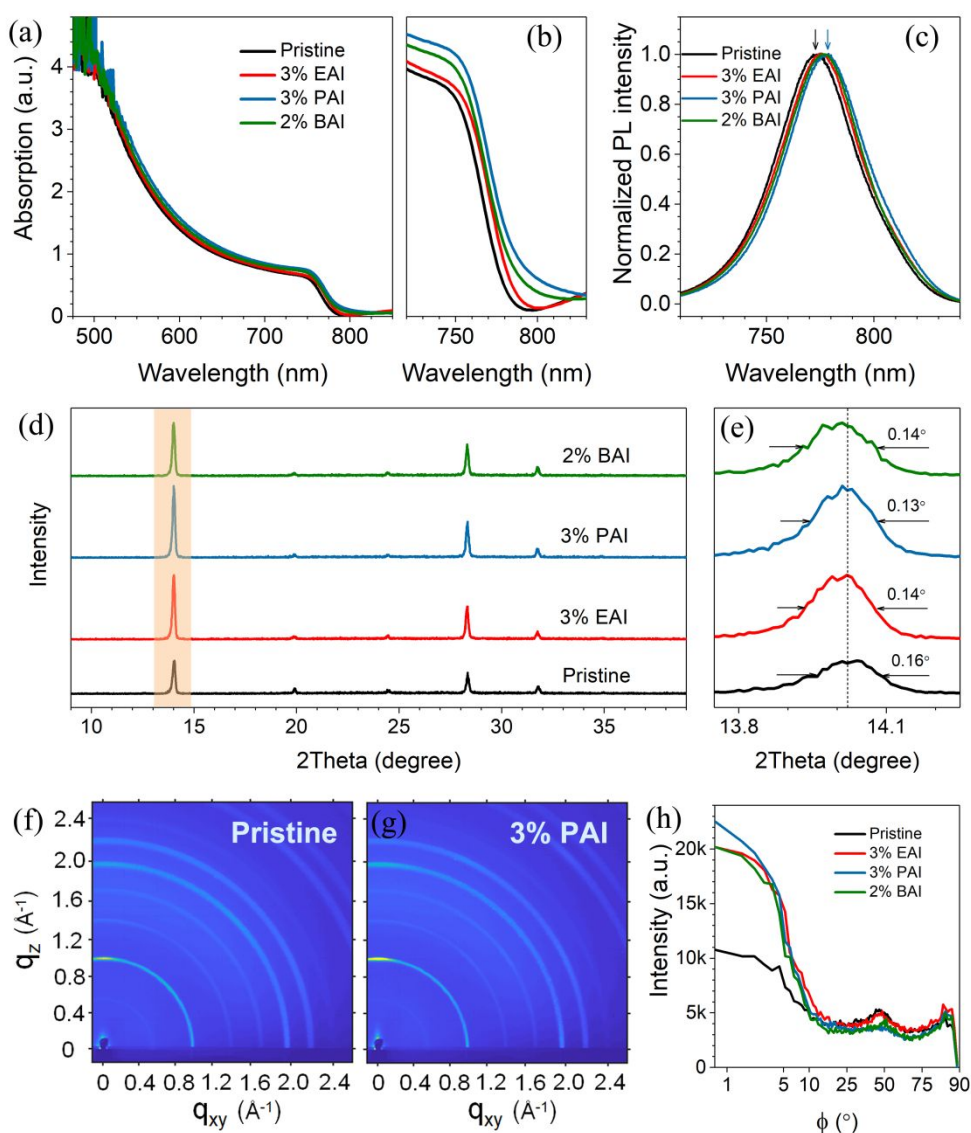


Fig. 1 (a)-(b) The steady-state absorption and (c) steady-state photoluminescence spectra of the perovskite films fabricated from different precursors. (d) XRD patterns of the films and (e) selected range of plane (001). GIWAXS images of the (f) pristine and (g) 3% PAI films; (h) intensity as a function of azimuthal angle for $q = 1.0 \text{ \AA}^{-1}$.

we use femtosecond transient absorption and reflection halide anion X. $n = 1$ and $n = \infty$ correspond to pure 2D and

pure 3D OIHPs, respectively, while all other n values (2, 3, 4, 5...) are referred to as quasi-2D OIHPs.³⁶ The pristine sample without a spacer cation is $\text{Cs}_{0.05}\text{FA}_{0.80}\text{MA}_{0.15}\text{Pb}(\text{I}_{0.85}\text{Br}_{0.15})_3$. In order to compare the effects of different cations, we chose 3% EA (in mol ratio relative to Pb), 3% PA, and 2% BA. 3% and 2% in mol are equivalent to $n = 67$ and $n = 100$, respectively. The selection of such ratio is based on the compositional optimization of device efficiency (Fig. S1, S2, Table S1).

Fig. 1a shows the ultraviolet-visible (UV-vis) absorption spectra for a pristine film as well as OIHP films containing 3% EA, 3% PA, and 2% BA, respectively. With the exception of the absorption edge (Fig. 1b), the OIHP films possess similar profiles over the entire visible regime. Compared with the pristine sample, the absorption edge is red-shifted from 781.2 nm to 786.4 nm when EA is added and further red-shifted to 787.6 nm when PA is incorporated. With the addition of BA, the absorption edge is 786.5 nm, slightly blue-shifted relative to PA, but still red-shifted relative to the pristine sample. The red shift with the incorporation of large cations is surprising, given that 2D perovskites exhibit a larger band gap. The literatures have reported both red shift and blue shift.^{10, 23, 24, 37} As shown in Fig. S3, the red shift of PA cation introduced in MAPbI_3 film is not obvious and sensitive to the background. The red shift is smaller than that in the multiple ion perovskite. Therefore, we speculate that this red shift is related with the component of perovskite, since the variation of I/Br ratio can change the bandgap of perovskite film. Besides the component and composition, the perovskite film with high crystallinity has narrowed effective optical bandgap, resulting in the red shift of the absorption edge.³⁸ The steady-state photoluminescence (PL) signals for these films after the addition of large cations in particular PA are also red-shifted (773 nm for pristine, 776 nm for EA, 779 nm for PA, and 777 nm for BA) (Fig. 1c). This trend is consistent with the steady-state absorption result. Fig. 1d summarizes the X-ray diffraction (XRD) patterns of a pristine film and those with different cations. The pristine film shows two major peaks at 14.1° and 28.2° , corresponding to the crystallographic planes of (001) and (002), respectively, of the 3D perovskite FAPbI_3 .³⁹ After adding EA, PA, and BA, the intensities of two peaks are significantly enhanced, suggesting higher degree of crystallinity. Since the large cations tend to form both at the film surface and the grain boundaries via self-assembly, the large cation can tighten the perovskite domains and passivate the surface defect.²⁴ The full width at half maximum (FWHM) of the (001) peak decreases after the addition of large cations (Fig. 1e), while the peak position moves slightly towards low angle, indicating an increased crystallite size and reduced residual stress.⁴⁰ This is consistent with the picture that the large cations at the grain boundaries tighten the FAPbI_3 domains.

XRD studies may be used to gain structural insights, compare the crystallinity and crystallite size, however, it does not provide a conclusive determination of the crystal preferential orientation with respect to the substrate. Therefore, we utilized grazing-incidence wide-angle X-ray scattering (GIWAXS) to determine crystal orientation upon the incorporation of large cations within the perovskite bulk.⁴¹ Fig.

1f shows the GIWAXS image of a pristine perovskite film. GIWAXS scattering peak assignments corroborate the formation of a crystalline layer with its most intense scattering peaks corresponding to reflections associated with the (001) and (002) crystallographic planes at $q = 1.0 \text{ \AA}^{-1}$ and $q = 2.0 \text{ \AA}^{-1}$, respectively.⁴² Fig. 1g displays the GIWAXS image of a perovskite film containing PA as the large cation (GIWAXS images for other samples are presented in Fig. S4). The GIWAXS patterns presented in Fig. 1f and 1g also demonstrate anisotropic intensities around the (001) family of planes. In particular, the (001) reflection is most intense at the meridian ($q_{xy} = 0$), an indication that the (001) planes are preferentially oriented normal to the substrate. An alternative means of quantifying the extent by which the crystallite orientation within the perovskite layer is affected upon introducing large cations may be achieved by determining the intensity of the (001) with respect to the azimuth. Figure 1h displays the intensity as a function of azimuthal angle Φ for $q = 1.0 \text{ \AA}^{-1}$ for a pristine film and for those films with different cations. We observe that the intensity at $\Phi = 0^\circ$ for the film with PA is doubled compared to that of the pristine film. This intensity enhancement normal to the substrate is consistent with the trend shown in the vertical line cuts (Fig. S4b). Our results demonstrate that the addition of large cations enhances the crystallinity and preferential crystal orientation of the (001) plane normal to the substrate, with PA being the most

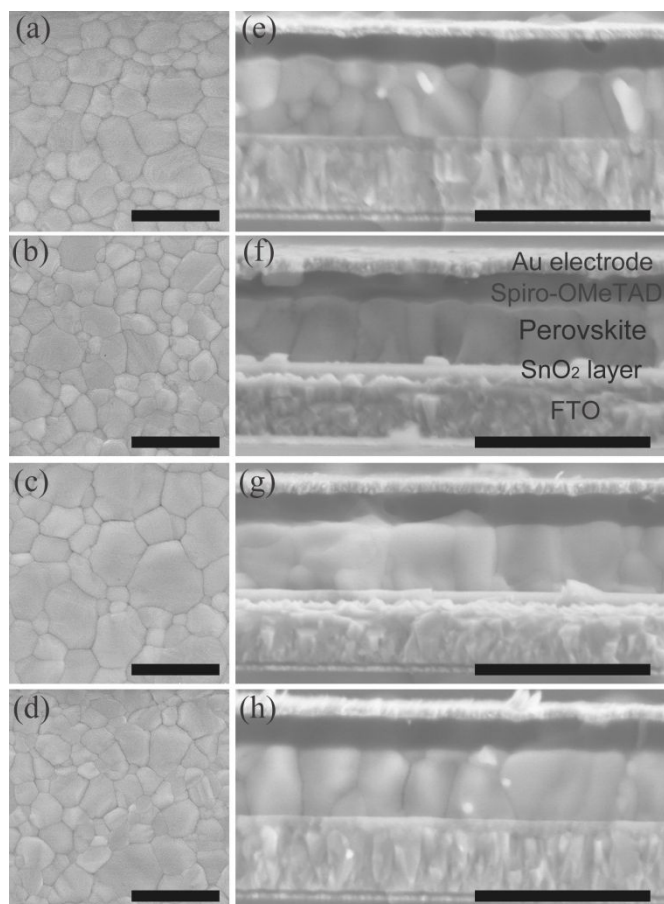


Fig. 2 SEM images of perovskite films: (a) pristine, (b) 3% EAI, (c) 3% PAI and (d) 2% BAI. (e)-(h) are the cross-sectional images. All the scale bars are 1 μm .

effective. Combining the results from absorption, PL spectra, XRD, and GIWAXS demonstrates that the introduction of small amounts of large cations increases the crystallinity and induces crystal preferential orientation. Changes observed upon the incorporation of PA cations into the perovskite matrix are more extensive than that observed for EA and BA.

If the crystallinity and the crystallite size increase, it should also follow that the grain size would be expected to become larger as well. This was studied with the use of scanning electronic microscopy (SEM) to observe and contrast the domain size of the pristine sample and those with the cations EA, PA, and BA (Fig. 2). Low magnification images are shown in Fig. S5 to show the film uniformity. The SEM top-view images with low and high magnifications show that the average domain size slightly increases from 490 nm (pristine) to 520 nm when 3% EA is added. The domain size further increases to 860 nm with the addition of 3% PA and slightly less than 710 nm with the addition of 2% BA. This trend is consistent with

the absorption, PL spectra, and X-ray results. From the cross-sectional SEM images, multiple domains are formed for the pristine sample along the surface normal (Fig. 2e) while the addition of EA, PA, or BA enables the formation of single domains in the vertical direction (Fig. 2f-2h). This is consistent with the GIWAXS results showing crystal preferential orientation in the vertical direction caused by large cations. As the charge carriers need to migrate along the surface normal, the suppression of grain boundaries in this direction can improve charge transport and suppress recombination.

As crystallization and grain size may affect both charge carrier transport and recombination, femtosecond transient absorption (TA) and transient reflection (TR) experiments were performed to study charge carrier dynamics in the bulk and at the surface. Fig. 3c-f display images of TA spectra, $\Delta T/T$ of the pristine perovskite film and those with different cations. The power of the pump laser at 400 nm was $10 \mu\text{J}/\text{cm}^2$. Two very distinct signals are observed. The positive signal arises from

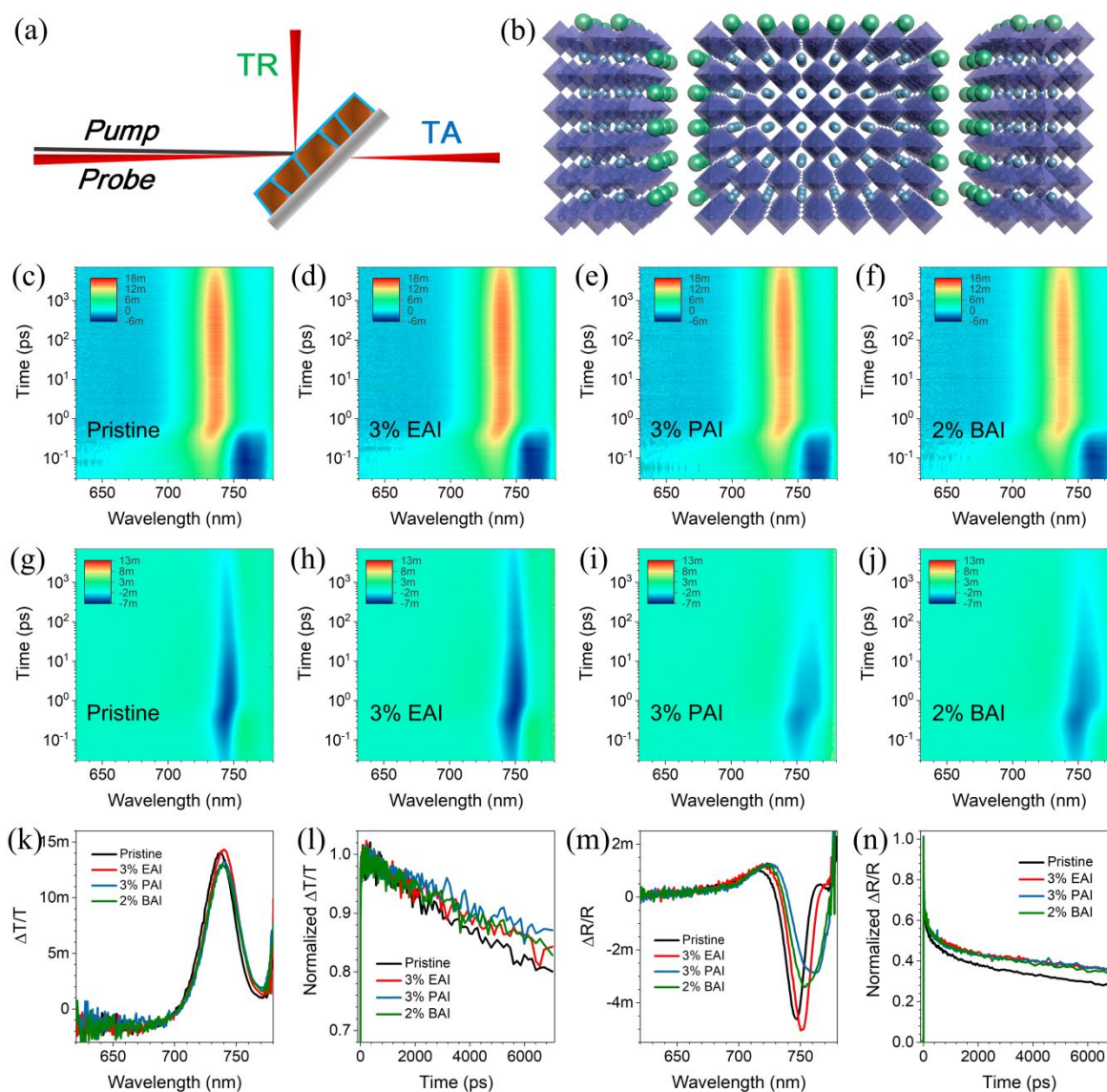


Fig. 3 Schematic illustrations of (a) TA and TR spectroscopy; (b) passivation of grain boundaries and film surface by large cations (green balls). (c)-(f) TA spectra and (g)-(j) TR spectra of perovskite films. (k) The spectra at 10 ps and (l) kinetics collected from TA spectra of perovskite films with and without large cations. (m) The spectra at 10 ps and (n) kinetics collected from the TR spectra of above films.

ground state bleaching and stimulated emission, and the negative signal arises from excited state absorption.⁴³⁻⁴⁵ While the spectra of these films are comparable with peaks located from 737 to 740 nm (Fig. 3k), the kinetics however are slightly different (Fig. 3l). The curves were fit with bi-exponential function with rise from hot carrier cooling and single exponential decay (Table S2, Fig. S6). The slightly slower decay through the addition of cations can be attributed to the passivation of the grain boundaries.

TA spectroscopy collects the probe signal transmitted through the entire sample, giving a signal that is integrated over the whole sample. Most importantly, TR spectroscopy collects probe pulses in the reflection geometry causing it to be sensitive to the top 20 nm from the surface (schematic illustration in Fig. 3a).⁴⁶ In contrast to the well-studied recombination in the bulk, surface recombination is still at the early stage. The carrier lifetime of the thin film is limited by surface recombination rather by bulk recombination, highlighting the importance of quantifying the surface carrier lifetime and surface passivation.⁴⁶ Fig. 3g-j display images of TR

spectra, $\Delta R/R$ of the pristine film and those with different cations. Fig. 3m and 3n summarize the spectra and kinetics for perovskite films without and with large cations from TR spectroscopy. The negative feature arises from ground state bleaching and stimulated emission, and the positive feature arises from excited state absorption.

The difference between TA and TR spectra suggests a photoinduced change of the refractive index.^{46, 47} We find that the spectra are obviously different when we add EA, BA, or PA, indicating that the small amount of large cations preferentially accumulates at the surface, forming a heterostructure. We observe that different cations induce ground state bleaching peaks red shifted to different extents with samples containing PA being the most prominent. For example, compared with the peak position at 747 nm for the pristine sample, the addition of EA and BA yield a red shift to 751 nm and 754 nm, respectively. The addition of PA yields the most pronounced red shift to 762 nm. This is consistent with the trend from steady-state absorption and PL spectra, but shows a more significant difference, indicating the differences between

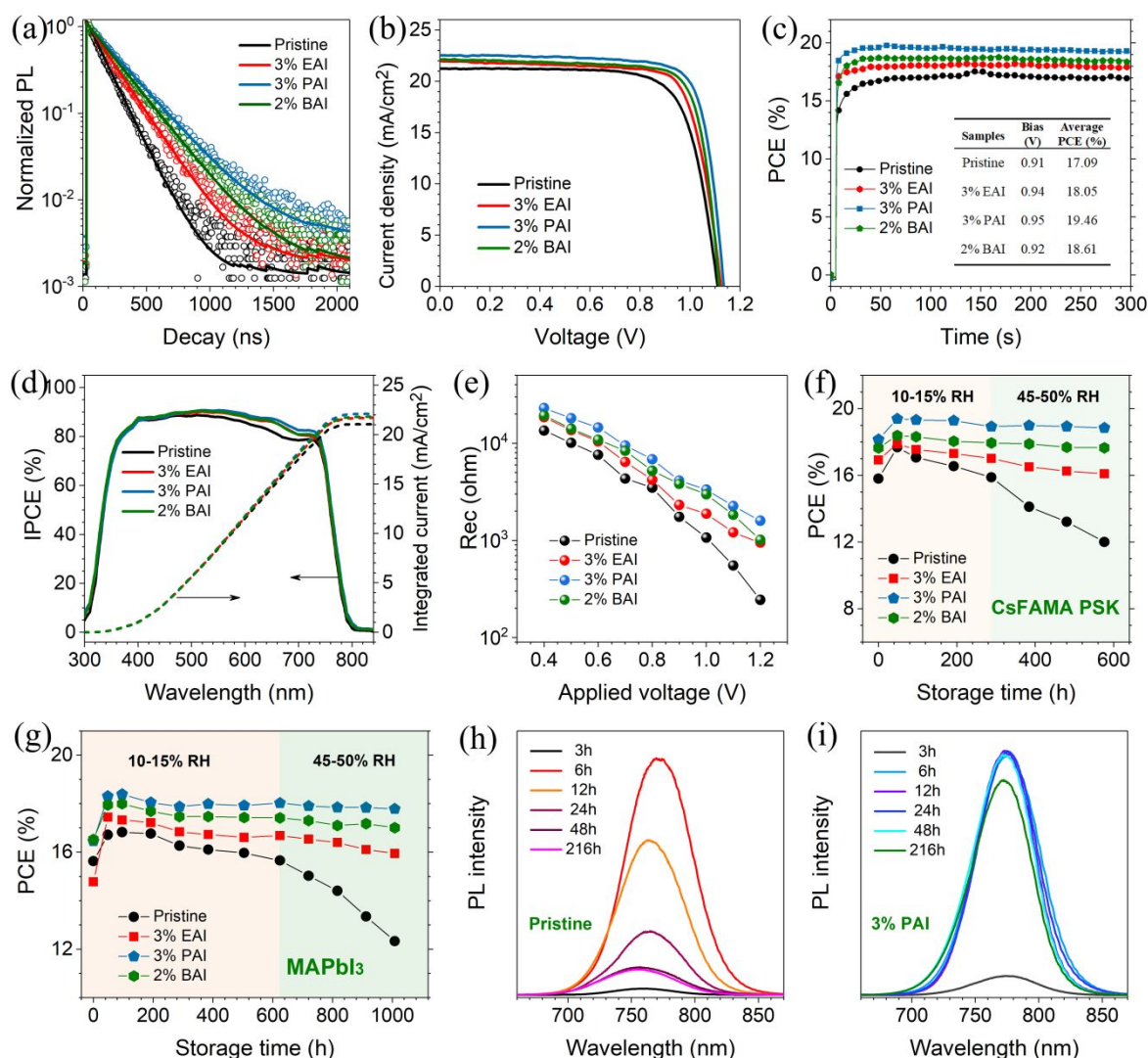


Fig. 4 (a) Time-resolved PL at 775 nm obtained for perovskite films upon excitation at 405 nm. (b) J-V curves of perovskite solar cells with different precursors. (c) Steady-state power conversion efficiency of perovskite solar cells (the average PCE is calculated from 50 to 300 s). (d) IPCE spectra of perovskite solar cells and integrated J_{sc} with and without cations. (e) R_{rec} of the solar cells extracted from EIS under different biases. Unencapsulated device stability for (f) mixed ion and (g) $MAPbI_3$ perovskite cells with and without large cations. Steady-state PL of (h) pristine films and (i) those treated by PAI from precursors with different aging times.

samples are largely from the film surface. Furthermore, the kinetic behaviour is different depending on the cation added to the perovskite matrix. The decays in the TR spectra are much faster than those in the TA spectra, indicating that the density of surface trap states is higher than that of the bulk. The lifetime is prolonged when large cations are incorporated with PA being the most noticeable. The fitting parameters for the curves are shown in Table S3 and Fig. S6. These suggest that the large cations that are self-assembling at the surface can prolong the surface carrier lifetime (Fig. 3b). This is consistent with the picture that a C-rich surface is better for passivation than Pb-rich.⁴⁶ Given that interfacial trapping is an essential limitation for solar cell devices, we believe that this surface capping with large cations not only prevents moisture from penetrating the perovskite matrix, but also benefits device efficiency. According to the similar valence band maxima of 2D and 3D OIHPs,^{12, 48} hole transport from 3D to 2D is allowed, while electron transport from 3D to 2D is blocked due to the unfavorable energy direction and large potential difference of conductive band. We believe the assembly of large cations at the surface can block electron transfer but assist hole transfer from the perovskite to hole transport layer.

Aside from femtosecond laser spectroscopy, time correlated single photon counting (TCSPC) was used to characterize the time-resolved PL (Fig. 4a). The PL decay trace was fit by single exponential decay convoluted with the instrumental response. The lifetime is increased from 143 ns to 206 ns, 267 ns, and 239 ns, after the addition of EA, PA, and BA, respectively. This trend is consistent with the enhanced crystallinity and crystal orientation measured by X-ray experiments and the larger domain size observed by SEM.

To study the effect of the incorporation of large cations into the perovskite active layer on device performance, we constructed OIHP conventional solar cells with both mesoporous and planar structures. The device with mesoporous structure has an architecture of FTO/TiO₂ compact layer/TiO₂ mesoporous/Perovskite/Spiro-OMeTAD/Au. We observe the efficiency generally increases by the addition of different cations, as shown in Fig. 4b (parameters in Table S4). Devices comprising only pristine perovskite layers displays an average short-circuit current density (J_{sc}) of 21.3 ± 0.4 mA/cm², open-circuit voltage (V_{oc}) of 1.11 ± 0.01 V, fill factor of 0.73 ± 0.02 , resulting in an average efficiency of 17.2 ± 0.5 %. By adding 3% EA, the average efficiency slightly increases to 18.3 ± 0.6 %. The addition of 3% PA further increases the average efficiency up to 19.7 ± 0.6 % and best efficiency to 20.3%. When compared to the addition of PA, the average efficiency drops to 18.7 ± 0.8 % with the addition of 2% BA. The efficiencies obtained from the J-V curves are consistent with the steady-state efficiencies (Fig. 4c). Similar efficiency trend by the addition of different cations is also observed for the device with planar structure FTO/SnO₂/perovskite/Spiro-OMeTAD/Au (Fig. S7 and Table S5). The hysteresis can also be suppressed by the addition of cations. The efficiency enhancement in both mesoporous and planar structures suggests the incorporation of small amount PA relative to other cations is more efficient in increasing the

device performance due to the enhanced crystallinity, crystal preferential orientation, larger domain size, and slower carrier decay.

Incident photon conversion efficiency (IPCE) spectra of the devices can be seen in Fig. 4d. With the inclusion of different cations, the traces at long wavelength show enhancement when compared to the pristine perovskite. An integrated J_{sc} is 21.1 mA/cm² for the pristine device and 22.1 mA/cm² for the PA device, consistent with the values measured from the J-V characteristics. The trend of integrated J_{sc} from IPCE for devices with different cations also matches with that determined by the J-V curves.

With the understanding that the large cations are segregated at the film surface and grain boundaries (Fig. 3b), such assemblies can passivate defects likely existing at the surface and grain boundaries. To further understand the carrier dynamics in functional devices, we carried out electrochemical impedance spectroscopy (EIS) studies to extract the recombination resistance (R_{rec}) for pristine devices and those with different cations under multiple biases in the dark. R_{rec} at different biases can be extracted from the Nyquist plots (Fig. S8). The obtained data in Fig. 4e is extracted based on the equivalent circuit model in which a recombination resistance R_{rec} is in parallel with a capacitance and then in series with a resistance. R_{rec} can originate from the recombination in the bulk and grain boundaries of the perovskite layer, charge transport layers, and the interfaces between adjacent layers.⁴⁹ The R_{rec} is largest for devices with PA and smallest for pristine devices, consistent with the efficient passivation by PA proved by time-resolved PL, TA and TR spectroscopy. The linear fit in Fig. 4e according to Equation 1 gives the ideality factor m .⁵⁰

$$\frac{d \log(R_{rec})}{dV} = \frac{e}{2.303mk_B T} \quad (1)$$

where k_B is the Boltzmann constant, T is the temperature, e is the electron charge, and V is the voltage. When $m = 1$, trap-assisted recombination is the dominant process; when $m = 2$, electron-hole recombination is the dominant process.^{51, 52} We extract $m=1.01, 1.08, 1.14$, and 1.13 for the pristine device and devices with EA, PA, and BA, respectively. The pristine device has a sharper slope (m closer to 1), suggesting that there are more trap states in the pristine device than in those with the cations. This is consistent with the picture that large cations passivate the trap states at the grain boundaries and the surface.

The device stability without encapsulation in low humidity (10-15% RH) and high humidity (45-50% RH) was tested for mixed ion OIHPs treated without and with different cations (EA, PA, and BA) (Fig. 4f). During the measurement process, the highest efficiency of the devices appeared at 2~4 days, which has been attributed to the age-induced recrystallization of perovskite.⁵³ As expected, different cations enhance the device stability of mixed ion perovskite solar cells with PA yielding the most stable devices. For example, the efficiency of pristine mixed ion perovskite decreases by 32.1% (from the highest efficiency) while those with PA only decrease by 2.8%

after 600 hours. To examine whether this stability improvement is also applicable for other perovskites, we carry out similar studies on another type of commonly studied perovskite MAPbI₃. Similarly, the efficiency of the pristine MAPbI₃ cell decreases by 26.7% while those with PA treatment only decrease by 5.5% after 1000 hours (Fig. 4g).

Aside from increasing device stability, interestingly, we also find that the precursor becomes more stable when large cations are added to the solution. Fig. 4h and 4i show the steady state PL of solid thin film treated without and with PA cations, respectively, from precursors with different aging times. The PL of the pristine film is very sensitive to the aging time of the precursor, while the film treated by PA cations is not sensitive to the aging time of the precursor. This indicates that the PA cations can also stabilize the precursor, leaving a large preparation window for the precursor before its use. We suspect that PA could be absorbed at the surface of perovskite colloid as a ligand, slowing down the phenomenon of Ostwald ripening (small particles aggregate into large particles) to improve the precursor stability. As shown in Fig. S9, the device performance of 3% PAI contained solar cells (20.1%) changed to 18.7% during the precursor aging process, while the efficiency of pristine device was dramatically decreased after 9 days' aging process (from 18.0% to 13.8%).

Conclusions

In summary, we demonstrate that the addition of small amounts of different cations, in particular PA, can passivate the grain boundaries and film surface by comparing TA and TR spectroscopy. Such assemblies can improve the grain size in both the lateral and vertical direction, crystal preferential orientation, and suppress the recombination, ultimately improving device efficiency. This passivation can prevent moisture diffusion, thus enhancing device stability. We also demonstrate that precursor stability can also be improved through the addition of PA cations.

Conflicts of interest

There are no conflicts to declare.

Acknowledgements

H. W. thanks the financial support by the Air Force Office of Scientific Research (AFOSR) under award No. FA9550-17-1-0099. L.W-B. would also like to acknowledge support by the AFOSR under award No. FA9550-18-1-0212. GIWAXS studies were conducted at CHESS, which is supported by the National Science Foundation (NSF) under award No. DMR-1332208.

References

- Best Research-Cell Efficiency Chart, <https://www.nrel.gov/pv/assets/pdfs/best-research-cell-efficiencies.pdf>, Accessed Dec. 21, 2018.
- Q. Chen, N. De Marco, Y. M. Yang, T.-B. Song, C.-C. Chen, H. Zhao, Z. Hong, H. Zhou and Y. Yang, *Nano Today*, 2015, **10**, 355-396.
- H. J. Jung, D. Kim, S. Kim, J. Park, V. P. Dravid and B. Shin, *Adv. Mater.*, 2018, **30**, 1802769.
- X. Zhao and N.-G. Park, *Photonics*, 2015, **2**, 1139-1151.
- A. M. A. Leguy, Y. Hu, M. Campoy-Quiles, M. I. Alonso, O. J. Weber, P. Azarhoosh, M. van Schilfgaarde, M. T. Weller, T. Bein, J. Nelson, P. Docampo and P. R. F. Barnes, *Chem. Mater.*, 2015, **27**, 3397-3407.
- Z. Song, A. Abate, S. C. Watthage, G. K. Liyanage, A. B. Phillips, U. Steiner, M. Graetzel and M. J. Heben, *Adv. Energy Mater.*, 2016, **6**, 1600846.
- J. Yang, B. D. Siempelkamp, D. Liu and T. L. Kelly, *ACS Nano*, 2015, **9**, 1955-1963.
- Q. Wang, B. Chen, Y. Liu, Y. Deng, Y. Bai, Q. Dong and J. Huang, *Energy Environ. Sci.*, 2017, **10**, 516-522.
- Y. Chen, Y. Sun, J. Peng, J. Tang, K. Zheng and Z. Liang, *Adv. Mater.*, 2017, **30**, 1703487.
- P. Gao, A. R. Bin Mohd Yusoff and M. K. Nazeeruddin, *Nat. Commun.*, 2018, **9**, 5028.
- L. Mao, C. C. Stoumpos and M. G. Kanatzidis, *J. Am. Chem. Soc.*, 2019, **141**, 1171-1190.
- G. Grancini and M. K. Nazeeruddin, *Nat. Rev. Mater.*, 2019, **4**, 4-22.
- Z. Li, M. Yang, J.-S. Park, S.-H. Wei, J. J. Berry and K. Zhu, *Chem. Mater.*, 2016, **28**, 284-292.
- J. C. Blancon, A. V. Stier, H. Tsai, W. Nie, C. C. Stoumpos, B. Traoré, L. Pedesseau, M. Kepenekian, F. Katsutani, G. T. Noe, J. Kono, S. Tretiak, S. A. Crooker, C. Katan, M. G. Kanatzidis, J. J. Crochet, J. Even and A. D. Mohite, *Nat. Commun.*, 2018, **9**, 2254.
- H. Tsai, R. Asadpour, J.-C. Blancon, C. C. Stoumpos, J. Even, P. M. Ajayan, M. G. Kanatzidis, M. A. Alam, A. D. Mohite and W. Nie, *Nat. Commun.*, 2018, **9**, 2130.
- I. C. Smith, E. T. Hoke, D. Solis-Ibarra, M. D. McGehee and H. I. Karunadasa, *Angew. Chem. Int. Ed.*, 2014, **126**, 11414-11417.
- L. N. Quan, M. Yuan, R. Comin, O. Voznyy, E. M. Bearegard, S. Hoogland, A. Buin, A. R. Kirmani, K. Zhao, A. Amassian, D. H. Kim and E. H. Sargent, *J. Am. Chem. Soc.*, 2016, **138**, 2649-2655.
- B.-E. Cohen, M. Wierzbowska and L. Etgar, *Adv. Funct. Mater.*, 2017, **27**, 1604733.
- J.-F. Liao, H.-S. Rao, B.-X. Chen, D.-B. Kuang and C.-Y. Su, *J. Mater. Chem. A*, 2017, **5**, 2066-2072.
- J. Lu, L. Jiang, W. Li, F. Li, N. K. Pai, A. D. Scully, C.-M. Tsai, U. Bach, A. N. Simonov, Y.-B. Cheng and L. Spiccia, *Adv. Energy Mater.*, 2017, **7**, 1700444.
- T. Niu, J. Lu, M.-C. Tang, D. Barrit, D.-M. Smilgies, Z. Yang, J. Li, Y. Fan, T. Luo, I. McCulloch, A. Amassian, S. Liu and K. Zhao, *Energy Environ. Sci.*, 2018, **11**, 3358-3366.
- S. Tan, N. Zhou, Y. Chen, L. Li, G. Liu, P. Liu, C. Zhu, J. Lu, W. Sun, Q. Chen and H. Zhou, *Adv. Energy Mater.*, 2019, **9**, 1803024.
- D. Q. Bi, P. Gao, R. Scopelliti, E. Oveisi, J. S. Luo, M. Gratzel, A. Hagfeldt and M. K. Nazeeruddin, *Adv. Mater.*, 2016, **28**, 2910-2915.
- N. Li, Z. Zhu, C.-C. Chueh, H. Liu, B. Peng, A. Petrone, X. Li, L. Wang and A. K. Y. Jen, *Adv. Energy Mater.*, 2017, **7**, 1601307.
- Y. Cho, A. M. Soufiani, J. S. Yun, J. Kim, D. S. Lee, J. Seidel, X. Deng, M. A. Green, S. Huang and A. W. Y. Ho-Baillie, *Adv. Energy Mater.*, 2018, **8**, 1703392.
- D. S. Lee, J. S. Yun, J. Kim, A. M. Soufiani, S. Chen, Y. Cho, X. Deng, J. Seidel, S. Lim, S. Huang and A. W. Y. Ho-Baillie, *ACS Energy Lett.*, 2018, **3**, 647-654.

- 27 R. Yang, R. Li, Y. Cao, Y. Wei, Y. Miao, W. L. Tan, X. Jiao, H. Chen, L. Zhang, Q. Chen, H. Zhang, W. Zou, Y. Wang, M. Yang, C. Yi, N. Wang, F. Gao, C. R. McNeill, T. Qin, J. Wang and W. Huang, *Adv. Mater.*, 2018, **30**, 1804771.
- 28 F. Li, Y. Zhang, K.-J. Jiang, C. Zhang, J.-H. Huang, H. Wang, H. Fan, P. Wang, Y. Chen, W. Zhao, X. Li, L.-M. Yang, Y. Song and Y. Li, *Adv. Mater.*, 2018, **30**, 1804454.
- 29 Y. Zhang, F. Li, K.-J. Jiang, J.-H. Huang, H. Wang, H. Fan, P. Wang, C.-M. Liu, L.-P. Zhang and Y. Song, *J. Mater. Chem. A*, 2018, **6**, 17867-17873.
- 30 Z. Wang, Q. Lin, F. Chmiel, N. Sakai, L. Herz and H. Snaith, *Nat. Energy*, 2017, **6**, 17135.
- 31 R. Quintero-Bermudez, A. Gold-Parker, A. H. Proppe, R. Munir, Z. Yang, S. O. Kelley, A. Amassian, M. F. Toney and E. H. Sargent, *Nat. Mater.*, 2018, **17**, 900-907.
- 32 W. F. Fu, J. Wang, L. J. Zuo, K. Gao, F. Liu, D. S. Ginger and A. K. Y. Jen, *ACS Energy Lett.*, 2018, **3**, 2086-2093.
- 33 J.-W. Lee, Z. Dai, T.-H. Han, C. Choi, S.-Y. Chang, S.-J. Lee, N. De Marco, H. Zhao, P. Sun, Y. Huang and Y. Yang, *Nat. Commun.*, 2018, **9**, 3021.
- 34 P. Li, Y. Zhang, C. Liang, G. Xing, X. Liu, F. Li, X. Liu, X. Hu, G. Shao and Y. Song, *Adv. Mater.*, 2018, **30**, 1805323.
- 35 H. Lai, B. Kan, T. Liu, N. Zheng, Z. Xie, T. Zhou, X. Wan, X. Zhang, Y. Liu and Y. Chen, *J. Am. Chem. Soc.*, 2018, **140**, 11639-11646.
- 36 D. H. Cao, C. C. Stoumpos, O. K. Farha, J. T. Hupp and M. G. Kanatzidis, *J. Am. Chem. Soc.*, 2015, **137**, 7843-7850.
- 37 Y. Lin, Y. Bai, Y. J. Fang, Z. L. Chen, S. Yang, X. P. Zheng, S. Tang, Y. Liu, J. J. Zhao and J. S. Huang, *J. Phys. Chem. Lett.*, 2018, **9**, 654-658.
- 38 Z. Chen, Q. Dong, Y. Liu, C. Bao, Y. Fang, Y. Lin, S. Tang, Q. Wang, X. Xiao, Y. Bai, Y. Deng and J. Huang, *Nat. Commun.*, 2017, **8**, 1890.
- 39 A. A. Zhumekenov, M. I. Saidaminov, M. A. Haque, E. Alarousu, S. P. Sarmah, B. Murali, I. Dursun, X. H. Miao, A. L. Abdelhady, T. Wu, O. F. Mohammed and O. M. Bakr, *ACS Energy Lett.*, 2016, **1**, 32-37.
- 40 M. Vashista and S. Paul, *Philos. Mag.*, 2012, **92**, 4194-4204.
- 41 Z. Jiang, *J. Appl. Crystallogr.*, 2015, **48**, 917-926.
- 42 G. Zheng, C. Zhu, J. Ma, X. Zhang, G. Tang, R. Li, Y. Chen, L. Li, J. Hu, J. Hong, Q. Chen, X. Gao and H. Zhou, *Nat. Commun.*, 2018, **9**, 2793.
- 43 H. Wang, L. Whittaker-Brooks and G. R. Fleming, *J. Phys. Chem. C*, 2015, **119**, 19590-19595.
- 44 H. Wang, L. Valkunas, T. Cao, L. Whittaker-Brooks and G. R. Fleming, *J. Phys. Chem. Lett.*, 2016, **7**, 3284-3289.
- 45 C. Fei, J. S. Sarmiento and H. Wang, *J. Phys. Chem. C*, 2018, **122**, 17035-17041.
- 46 Y. Yang, M. Yang, David T. Moore, Y. Yan, Elisa M. Miller, K. Zhu and Matthew C. Beard, *Nat. Energy*, 2017, **2**, 16207.
- 47 M. B. Price, J. Butkus, T. C. Jellicoe, A. Sadhanala, A. Briane, J. E. Halpert, K. Broch, J. M. Hodgkiss, R. H. Friend and F. Deschler, *Nat. Commun.*, 2015, **6**, 8420.
- 48 R. K. Misra, B.-E. Cohen, L. Iagher and L. Etgar, *ChemSusChem*, 2017, **10**, 3712-3721.
- 49 C. Fei, L. Guo, B. Li, R. Zhang, H. Fu, J. Tian and G. Cao, *Nano Energy*, 2016, **27**, 17-26.
- 50 C. Fei, B. Li, R. Zhang, H. Fu, J. Tian and G. Cao, *Adv. Energy Mater.*, 2017, **7**, 1602017.
- 51 M. Bernechea, N. C. Miller, G. Xercavins, D. So, A. Stavrinadis and G. Konstantatos, *Nat. Photonics*, 2016, **10**, 521-525.
- 52 W. J. Nimens, J. Ogle, A. Caruso, M. Jonely, C. Simon, D. Smilgies, R. Noriega, M. Scarpulla and L. Whittaker-Brooks, *ACS Appl. Energy Mater.*, 2018, **1**, 602-615.
- 53 C. Fei and H. Wang, *Org. Electron.*, 2019, **68**, 143-150.